

---

## A microfluidic mechano-chemostat for tissues and organisms reveals that confined growth is accompanied with increased macromolecular crowding

Ben Meriem Zacchari <sup>1</sup>, Mateo Tiphaine <sup>1</sup>, Faccini Julien <sup>1</sup>, Denais Céline <sup>1</sup>, Dusfour-Castan Romane <sup>2</sup>, Guynet Catherine <sup>2</sup>, Merle Tatiana <sup>3</sup>, Suzanne Magali <sup>3</sup>, Di-Luoffo Mickaël <sup>4</sup>, Guillermet-Guibert Julie <sup>4</sup>, Alric Baptiste <sup>1</sup>, Landiech Sylvain <sup>1</sup>, Malaquin Laurent <sup>1</sup>, Mesnilgrente Fabien <sup>1</sup>, Laborde Adrian <sup>1</sup>, Mazenq Laurent <sup>1</sup>, Courson Remi <sup>5</sup>, Delarue Morgan <sup>1,\*</sup>

<sup>1</sup> LAAS-CNRS, Université de Toulouse, CNRS, Toulouse, France

<sup>2</sup> Laboratoire de Microbiologie et de Génétique Moléculaires, Centre de Biologie Intégrative (CBI), CNRS, Université de Toulouse, F-31000, Toulouse, France

<sup>3</sup> Molecular, Cellular and Developmental Biology unit (MCD), Centre de Biologie Intégrative (CBI), Université de Toulouse, CNRS, UPS, France

<sup>4</sup> INSERM U1037, CRCT, Université de Toulouse, F-31037 Toulouse, France

<sup>5</sup> Ifremer, RDT, F-29280 Plouzané, France

\* Corresponding author : Morgan Delarue, email address : [morgan.delarue@laas.fr](mailto:morgan.delarue@laas.fr)

---

### Abstract :

Conventional culture conditions are oftentimes insufficient to study tissues, organisms, or 3D multicellular assemblies. They lack both dynamic chemical and mechanical control over the microenvironment. While specific microfluidic devices have been developed to address chemical control, they often do not allow the control of compressive forces emerging when cells proliferate in a confined environment. Here, we present a generic microfluidic device to control both chemical and mechanical compressive forces. This device relies on the use of sliding elements consisting of microfabricated rods that can be inserted inside a microfluidic device. Sliding elements enable the creation of reconfigurable closed culture chambers for the study of whole organisms or model micro-tissues. By confining the micro-tissues, we studied the biophysical impact of growth-induced pressure and showed that this mechanical stress is associated with an increase in macromolecular crowding, shedding light on this understudied type of mechanical stress. Our mechano-chemostat allows the long-term culture of biological samples and can be used to study both the impact of specific conditions as well as the consequences of mechanical compression.

## 36 **Introduction**

37 Cells in tissues and organisms, or during development, are constantly subjected to dynamic chemical  
38 and mechanical cues. Imposing dynamic chemical conditions on 3D cellular assemblies is a technical  
39 challenge **that** requires the use of complex microfluidic devices<sup>1-4</sup>. However, despite the large  
40 parallelization enabled by some of these devices, they do not necessarily allow easy dynamic  
41 control, and very few enable the establishment of chemical spatial gradients<sup>5,6</sup> which are essential  
42 to study 3D chemotaxis or drug screening. Mechanically, and apart from devices allowing control of  
43 shear or tensile stresses<sup>7,8</sup>, the appropriate 3D mechanical conditions to study the effect of spatial  
44 confinement and compressive stresses are lacking.

45  
46 Compressive stresses can either be dynamic, such as peristalsis during digestion or the compression  
47 of articular cartilage during motion<sup>9</sup>, or self-inflicted in the case of spatially constrained growth<sup>10</sup> –  
48 **the so-called growth-induced pressure**. Indeed, compressive stress naturally arises when cells  
49 proliferate in a confined space, like solid tumors growing within an organ<sup>11</sup>. Compressive stresses  
50 can be deleterious for tumor treatment since they can clamp blood vessels<sup>12</sup>, modulate cell  
51 proliferation<sup>13-15</sup>, and even participate in a mechanical form of drug resistance<sup>15</sup>. In contrast with  
52 tensile and shear stresses<sup>16-21</sup>, very little is known about the sensing of mechanical pressure.

53  
54 Growth-induced pressure is notoriously hard to study. **Current methods to impose spatial**  
55 **confinement either rely on open-facing devices<sup>22</sup> or spheroid embedding in a hydrogel<sup>13-15</sup>. While**  
56 **hydrogel embedding** displays natural limitations in terms of the type and size of the studied sample  
57 **as well as** its retrieval for further biological characterization and the dynamic control of the culture  
58 conditions, **open-facing devices do not fully confine tissues which can grow in the third dimension,**  
59 **leading to a poor buildup of growth-induced pressure in the Pa range<sup>23</sup>, far from the typical kPa**  
60 **range of pressure measured during hydrogel embedding<sup>15</sup>.**

61  
62 In general, the culture of organisms inside microfluidic devices remains difficult to do, even though  
63 microfluidic systems can offer much tighter control than classical culture. In this paper, we present  
64 **a generic microfluidic device** that takes advantage of an innovative technology called sliding  
65 elements. Sliding elements are microfabricated rods that can be inserted inside a microfluidic  
66 device. Using this technology, we created reconfigurable **easy-to-use confining** culture chambers  
67 which could be loaded with biological objects such as spheroids **in order to study the impact of**  
68 **growth-induced pressure**. This device permits great chemical and mechanical control, real-time

69 imaging, and the possibility to recover the sample. Novel pressure sensors have been developed to  
70 measure growth-induced pressure. We demonstrated that our device was fitted for the controlled  
71 culture of multicellular spheroids, and showed that growth-induced pressure was associated with  
72 increased macromolecular crowding, thus shedding light on a novel biophysical regulation of  
73 confined growth in mammalian cells. Prospectively, we showed that our device can be used for the  
74 culture of other organisms, such as the nematode *C. elegans* or imaginal discs of the *D.*  
75 *melanogaster*.

76

## 77 **Results**

### 78 ***Sliding elements to create a microfluidic chemostat for biological samples***

79 The realization of a microfluidic chemostat resides in our ability to load a sample at a given position  
80 and define the chemical environment around it (Fig. 1a). Valves could be used to trap a sample, but  
81 the feeding remains difficult. Solutions relying on one-way valves have been developed for  
82 microbes<sup>10,24</sup>, but are not directly amenable to larger and deformable samples. To overcome this  
83 difficulty, we underwent a key technological development: sliding elements, tiny 3D-structured rods  
84 which can be inserted inside a microfluidic system to bring specific functions of interest<sup>25</sup>. By  
85 coupling standard photolithography and the use of dry film photoresists, we created well-defined  
86 and transparent sliding elements with cylindrical holes or slits depending on the direction of  
87 fabrication (Fig. 1b). They were centimetric in length and squared in the other dimensions with a  
88 cross size of 500 $\mu$ m, making them easy to manipulate and slide into a designated channel (Fig. 1c).  
89 We created them by the hundreds in one batch (Fig. 1d, inset).

90

91 Culture chambers were molded in polydimethylsiloxane (PDMS) from molds created using multi-  
92 level photolithography, the first one defining the height of the culture chamber, while the second  
93 one delineated the channel into which the sliding element would be inserted (Fig. 1c). The height of  
94 this channel had to be optimized to ensure tight sealing and avoid medium leakage from one  
95 compartment to the next. We find that the channel with the sliding element did not leak for fluid  
96 pressure below 200 kPa, which was above the typical maximum 50 kPa pressure needed in our  
97 experiments to culture cells (Fig. S1). The leakage occurred along the sliding element, probably  
98 because of slight misalignment during the fabrication process, and even at 200kPa, no liquid went  
99 through the main channel. This tight sealing was essential to enable perfect control over the  
100 chemical environment. Notably, we showed that we could instantaneously change the chemical  
101 conditions in the chamber (Fig. S2). We could have a fresh medium with constant chemical

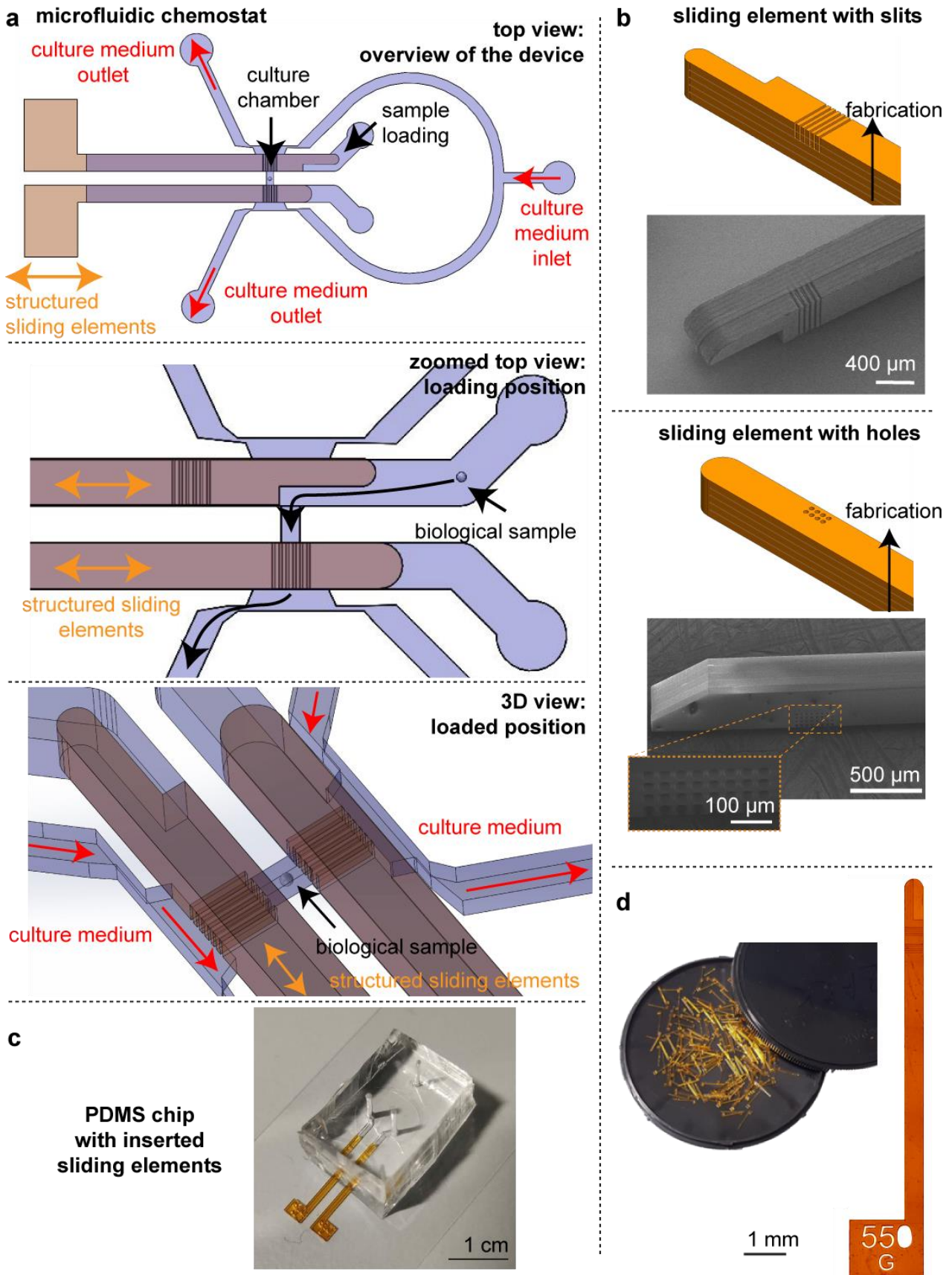


**Figure 1: Design of the microfluidic chemostat.** **a.** The microfluidic chemostat is composed of a culture chamber that is closed on both sides by structured sliding elements. These elements enable to load the chamber and feed the sample thanks to channels on both sides. **b.** Standard photolithography is used on dry films to structure in 3D the element. Depending on the direction of construction, we can either construct slits or holes. Scanning electron images of the sliding elements are presented. **c.** Picture of the microfluidic device with the sliding elements inserted. **d.** The sliding elements are centimetric in length and structured at the tens of micrometer resolution. They are fabricated by the hundreds and can be inserted in a PDMS chip.

103 either decrease waste or perform specific enrichment experiments.

104

### 105 **Steady culture of multicellular spheroids**

106 The chemostat could be easily smoothly loaded with various biological objects. Sliding one element  
107 down opens one side of the chamber so that by adjusting the inlet flow, we could control the  
108 position of a multicellular spheroid inside the chamber, pushing it to the end, or retrieving it. We  
109 showed that spheroids can be cultured in the device for days (Fig. 2a and supplementary video S1),  
110 with no significant differences in growth measured inside the device in comparison with classical  
111 culture in well plates (Fig. 2b). Each replicate in Fig. 2b is made with a different PDMS chip, a  
112 different set of sliding elements, and a different spheroid, demonstrating the robustness and  
113 reproducibility of the experiments. Of note, we could parallelize the chambers, different spheroids  
114 could be loaded in different chambers (Fig. 2c), to increase throughput or parallelize experiments.  
115 Interestingly, we can also load two different samples in the same chamber (Fig. 2di-ii). This unique  
116 feature, which cannot be done in open-facing devices or in hydrogels, is of particular interest to

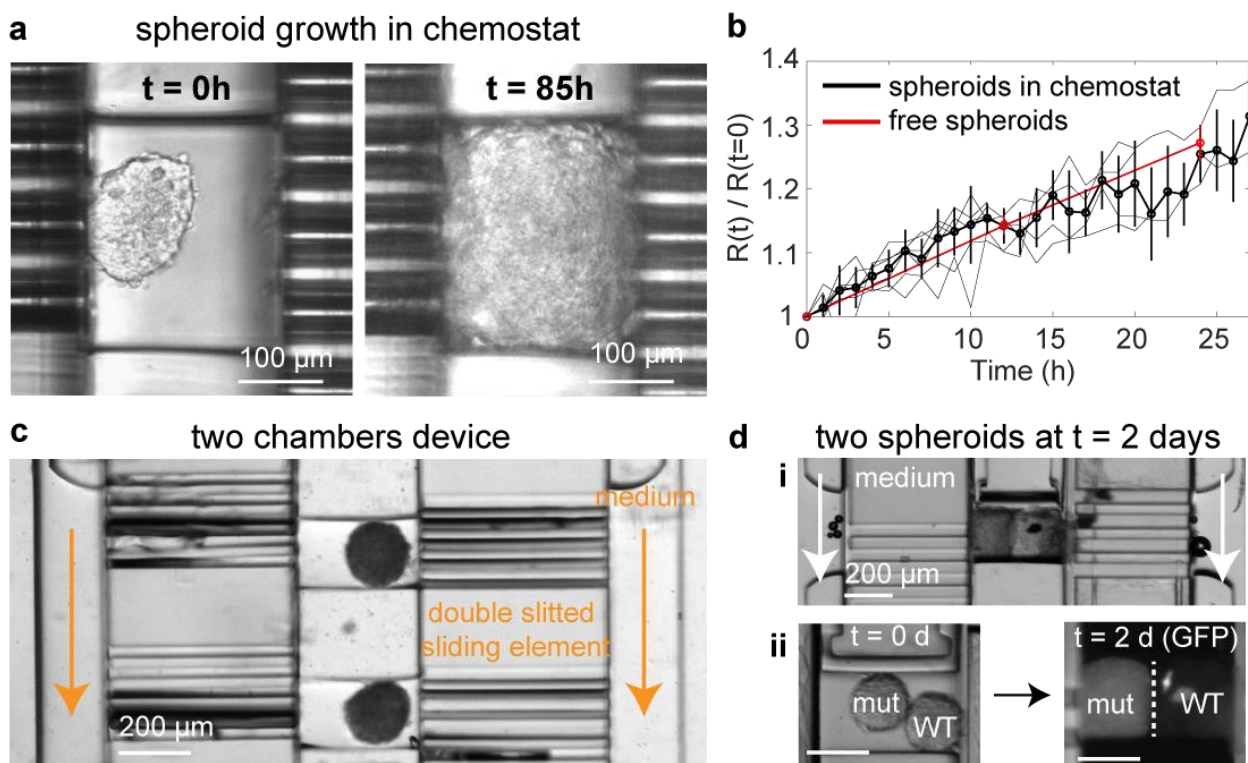


**Figure 2: Culture of multicellular spheroids in the microfluidic chemostat.** **a.** Multicellular spheroids can be loaded in the chemostat. They can grow until they fill the chamber. **b.** Growth curves of spheroids in the chemostat (6 independent replicates – unique spheroid, unique PDMS chip and unique set of sliding elements - in light black) and in classical round bottom well plates (mean  $\pm$  SEM). Thick lines represent median  $\pm$  standard deviation. **c.** We designed devices with two parallel chambers where different samples can be loaded and cultured. **d.** Two different spheroids can be loaded and cultured in the same chamber (i). They grow until the chamber is filled (ii).



117 study interactions (mechanical and chemical) between different samples, and perform mechanical  
118 competition for space<sup>26</sup>.

119

### 120 ***Confined proliferation and growth-induced pressure***

121 Fully confining cells would require to decrease the size of holes or slits in the sliding elements to  
122 avoid cells escaping from them. Cells are indeed able to migrate and deform through constrictions  
123 as small as 5 $\mu\text{m}$ <sup>27</sup>, which was a resolution not reachable during sliding element fabrication. To  
124 overcome this issue, we designed a three-layer system with a culture chamber connected on its side  
125 to much smaller channels (2 $\mu\text{m}$  x 2 $\mu\text{m}$  in cross-section) which fully blocked the spheroid (Fig. 3a).  
126 We adapted the design of the sliding element to load and close these chambers (Fig. 3b and  
127 supplementary video S2), and observed that spheroids grew fully confined in this geometry  
128 (supplementary video S3), without invading the side channels. Normal growth of the spheroid was  
129 measured before being spatially confined (Fig. 3c), suggesting optimal feeding.

130

131 Confined growth eventually leads to the buildup of growth-induced pressure<sup>28</sup>. Evaluating growth-  
132 induced pressure often relies on the measurement of the surrounding deformation<sup>13,15,29</sup>, or the  
133 deformation of exogenous sensors such as hydrogel beads<sup>30,31</sup>. Alternatively, micropillars have been  
134 widely used to measure kPa stresses exerted by moving cells<sup>32</sup> or growing spheroids in open-facing  
135 devices<sup>22,23</sup>, due to their high deformation when sufficiently thin. We adapted this technology to  
136 design a thin suspended membrane to measure growth-induced pressure (Fig. 3d). We performed  
137 finite element simulations to tune its dimensions to be sensitive to the kPa range<sup>15</sup> (Fig. 3e). We  
138 observed that at similar dimensions, a fully attached membrane was much less deformable than  
139 one attached only at the top (Fig. S3). In order to calibrate the mechanical properties of the PDMS,  
140 a crucial parameter to perfectly infer the pressure exerted onto the membrane from its  
141 deformation, we designed a fully attached membrane and measured its deformation with a fixed  
142 pressure. The deformation as a function of pressure was used to determine the mechanical  
143 properties of the PDMS of the chip thanks to finite element simulations, allowing the proper  
144 calibration of the mechanical properties (Fig. S4). Of note, we could also use this membrane to  
145 instantaneously compress a trapped multicellular spheroid or a collagen gel (Fig. S5).

146

147 We observed that the confined proliferation of a spheroid led to the progressive build-up of growth-  
148 induced pressure over the kPa range for several days (Fig. 3f and supplementary video S3). The  
149 dynamics did not depend on the width of the suspended membrane (Fig. 3g) and was very

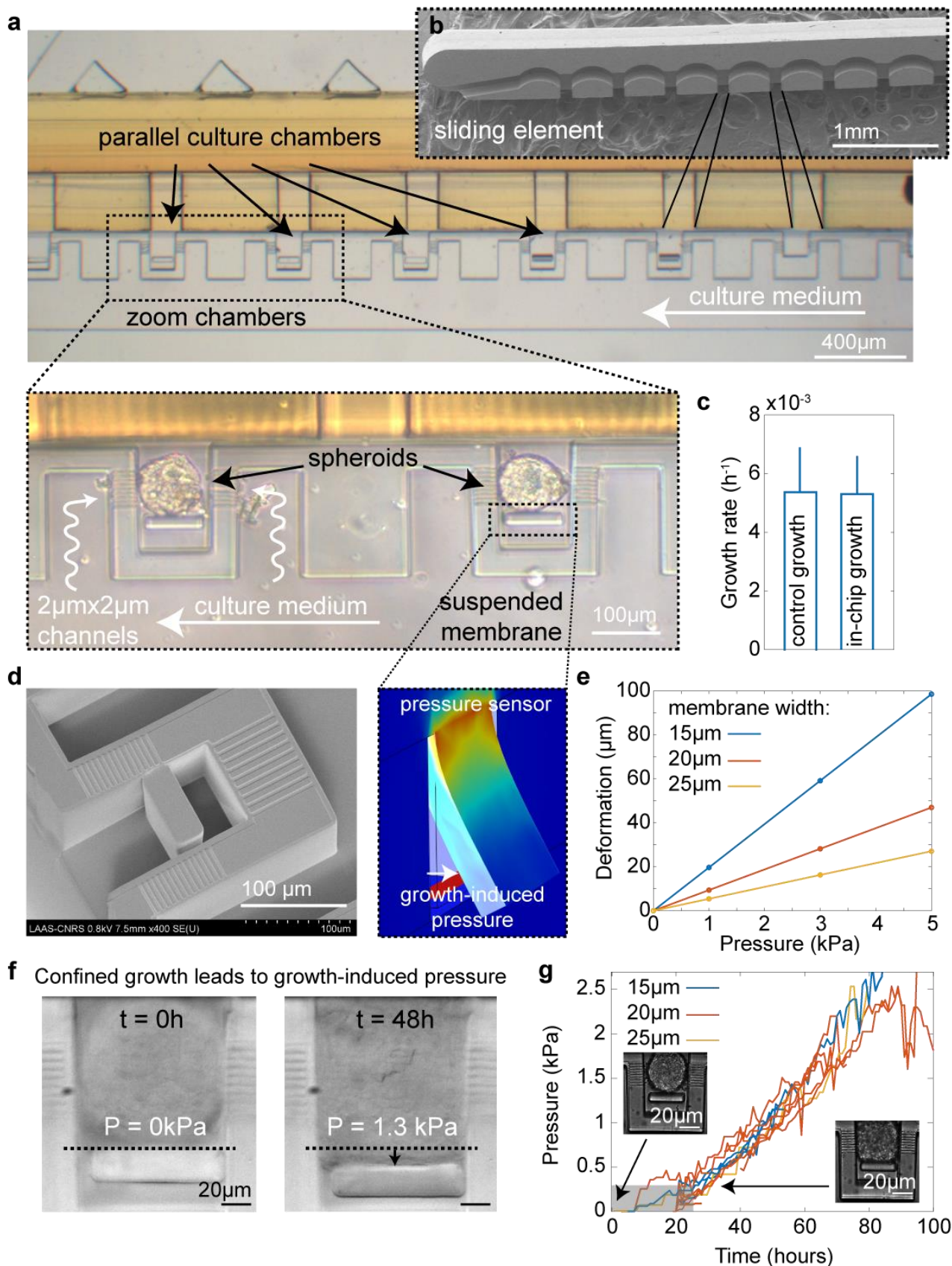


**Figure 3: Confined growth of multicellular spheroids and pressure sensor.** *a.* The design can be parallelized and built on three levels to create multiple closed culture chambers. *b.* The sliding element is structured in such a way as to allow the loading and closing of the chambers. *c.* The growth rate of multicellular spheroids before confinement is similar to that of free spheroids (median  $\pm$  standard deviation,  $N = 4$  independent experiments). *d.* Scanning electron microscope image of the chamber containing the suspended membrane. Image of a finite element simulation showing its deformation when a fixed pressure is applied. *e.* Deformation of the membrane with applied pressure as a function of membrane width. *f.* Confined growth leads to growth-induced pressure measured by the deformation of the suspended membrane. *g.* Pressure is independent of the width of the suspended membrane. After a slow increase which corresponds to a change of spherical shape to a cube, pressure increases roughly linearly for hours. The grayed area corresponds to the time points for which pressure is underestimated owing to the aggregate not fully contacting the surface. 10 spheroids over 4 independent experiments.

151 S6). This indicated that cells were similarly fed in both conditions and that growth-induced pressure  
152 development did not depend on the type of spatial confinement. Note that we needed to apply a  
153 correction factor when the spheroid did not fully contact the membrane (Fig. S7). Because this factor  
154 could not be easily determined with our imaging conditions, for pressures below 250 Pa, the  
155 pressure was underestimated – these points were grayed on the figure. Interestingly, we observed  
156 that during the first 24h, the spheroid deformed into a cuboid, while developing a growth-induced  
157 pressure of  $\sim 300$  Pa. We showed (see Methods) that this information can be used to quantify the  
158 surface tension of a spheroid, which in this case is in the range of 1.5 mN/m, consistent with  
159 measurements in other cell types done with classical micropipette aspiration<sup>33</sup>.

160

161 Importantly, the chambers can be re-opened to allow a non-chemical relaxation of the mechanical  
162 stress. The samples can be retrieved for further biological analysis, even after having been under  
163 mechanical pressure (Fig. S8). Note that the tissue remained cuboidal after being retrieved from the  
164 chamber. This essential point was often a bottleneck in microfluidics, and relaxing mechanical stress  
165 in hydrogel embedding systems requires the use of chemicals<sup>34</sup>, both of which the use of sliding  
166 elements easily overcame.

167

### 168 ***Growth-induced pressure increased intracellular crowding and decreased proliferation***

169 We sought to investigate the cellular response to growth-induced pressure. We measured cellular  
170 densification within the compressed tissue, suggesting that single cells were more compressed  
171 under confined growth (Fig. S9). Taking advantage of the fact that microfluidics allows high-  
172 resolution imaging, we used the Fucci cell-cycle marker (Fig. 4a) and measured a progressive  
173 accumulation of G1 cells as growth-induced pressure increased (Fig. 4b). This result was consistent  
174 with former findings showing an association between growth-induced pressure and physiological  
175 changes, and notably a decrease in cell proliferation<sup>13,15,29,34,35</sup>.

176

177 An elusive question in mechano-biology relates to how growth-induced pressure is integrated and,  
178 especially which cellular biophysical properties are modified. It has recently been shown in the  
179 budding yeast *Saccharomyces cerevisiae* that growth-induced pressure is accompanied by an  
180 increase in intracellular crowding<sup>28</sup>, which relates to the high packing fraction of macromolecules in  
181 cells<sup>36</sup>. Genetically-encoded multimeric nanoparticles (GEMs) can be imaged at the single cell level  
182 in order to infer intracellular crowding through single particle tracking<sup>37</sup> (Fig. 4c). Using GEMs, we  
183 sought to investigate how intracellular crowding was modified in mammalian cells during the



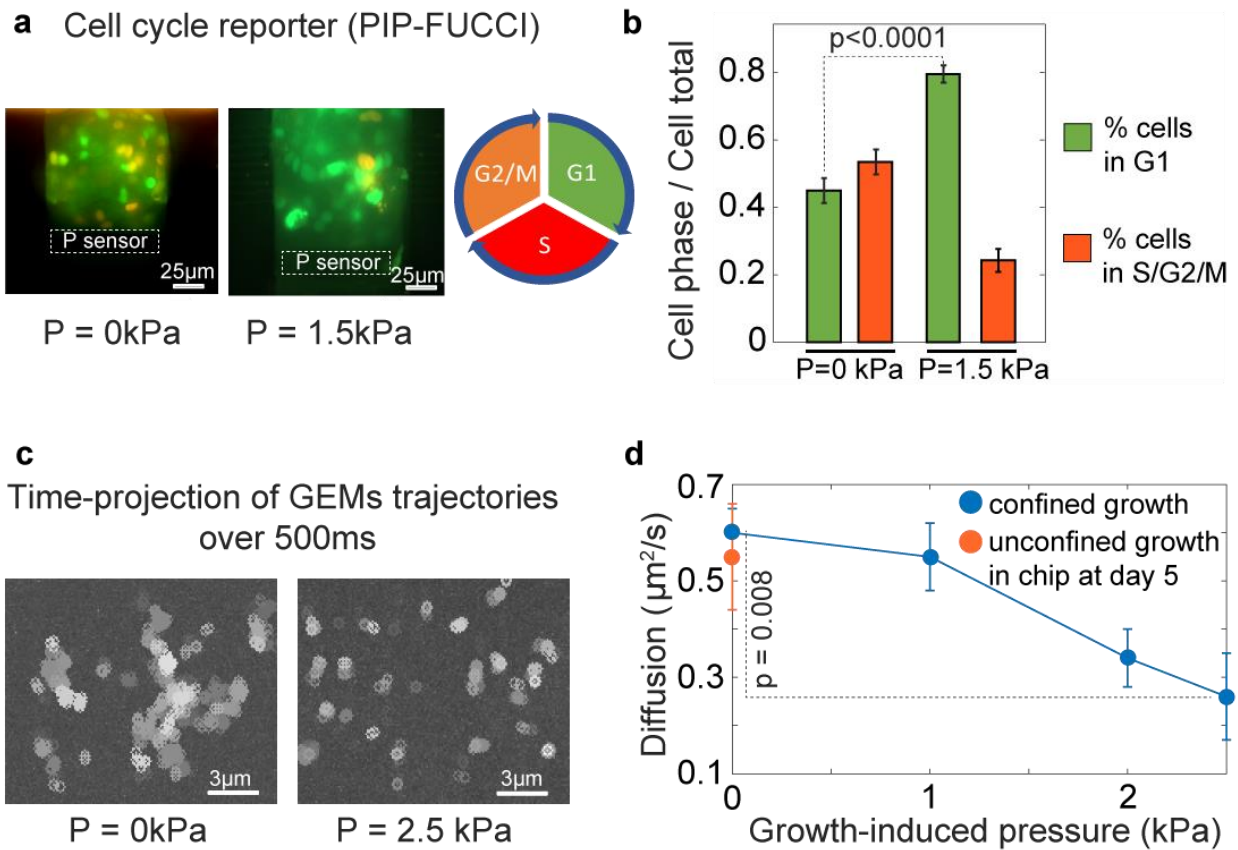


**Figure 4: Confined growth leads to growth-induced pressure which impacts cell proliferation and intracellular crowding.** *a.* Fucci cell cycle reporter to fluorescently label cell cycle phases. Representative images of Fucci-labeled cells in the device for different growth-induced pressure values. *b.* Cells accumulate in G1 as growth-induced pressure builds up. 6 spheroids over 4 independent experiments were analyzed. *c.* Time projection of GEMs nanoparticles trajectories shows that particles are less diffusive under growth-induced pressure. *d.* Diffusion progressively decreases as growth-induced pressure increases.  $N \geq 10$  cells for each point coming from 6 spheroids over 3 independent experiments. For all points, we computed the mean  $\pm$  standard error of the mean.

184 buildup of growth-induced pressure. We found that the mean diffusion coefficient was decreasing  
 185 with increased growth-induced pressure (Fig. 4d), suggesting that, similarly to *S. cerevisiae*,  
 186 intracellular crowding increased during confined proliferation and with the buildup of growth-  
 187 induced pressure. Note that the control condition of unconfined growth in the chip corresponded  
 188 to partial confinement of the spheroid: it was only allowed to grow in one direction, similar to what  
 189 happens in an open-facing device<sup>22</sup>. In this case, we noticed no change in the diffusion of the  
 190 nanoparticles, further illustrating the difference in the impact of full confinement in contrast to  
 191 partial one.

192

### 193 Conclusions

194 We reported in this article a generic microfluidic device allowing the controlled confined culture of  
 195 multicellular spheroids. Its operation relied on a key and novel technological development, sliding  
 196 elements, which could be inserted inside a PDMS device to create reconfigurable culture chambers.  
 197 Sliding elements could be produced by the hundreds, and allowed exquisite resolution thanks to the

198 power of photolithography. In particular, they could be structured by channels or holes, which  
199 allowed us to close a culture chamber while retaining the ability to feed the sample loaded in this  
200 chamber, something that a classical valve could not do.

201

202 The full confinement of a spheroid allows the study of growth-induced pressure. While hydrogel  
203 embedding can appear as an easier alternative, they do not offer the control that microfluidics  
204 permits. In particular, retrieving the spheroid after the experiment or relaxing growth-induced  
205 pressure without potential chemical stress is a challenge. Moreover, our device uniquely allows us  
206 to study the direct mechanical interaction of multicellular spheroids<sup>26</sup> (Fig. 2d), which is not possible  
207 through hydrogel embedding. Finally, open-facing systems do not fully confine spheroids, which  
208 leads to a poor buildup of mechanical stress and makes the study of this key mechanical stress  
209 impossible.

210

211 The confined growth of multicellular spheroids led to the buildup of growth-induced pressure, which  
212 has a number of physiological consequences. We developed a novel mechanical sensor to measure  
213 mechanical pressure and demonstrated that spheroids in our device could develop growth-induced  
214 pressure. In particular, their transition from a spheroid to a cuboid shape allows the estimation of  
215 the tissue surface tension independently of other viscoelastic and poromechanics parameters. How  
216 growth-induced pressure is integrated and impacts cells are mostly unknown, in contrast to other  
217 types of mechanical stresses, such as tensile<sup>16</sup> or shear<sup>21</sup>. We showed that while cell proliferation  
218 was decreased, as previously reported<sup>15,34</sup>, intracellular crowding increased concomitantly with  
219 growth-induced pressure in mammalian cells, yielding a novel biological insight on the mechanisms  
220 that can be associated with the integration of growth-induced pressure. To our knowledge, this is  
221 the first demonstration in mammalian cells that growth-induced pressure is associated with  
222 increased crowding. This was previously shown in the budding yeast *S. cerevisiae*<sup>28</sup>, raising the  
223 question of the universality of this phenomenon.

224

225 Our device could be used for the culture of other organisms. The system could be loaded with  
226 different organisms the same way a spheroid was (Fig. 1 and 2). Prospectively, we demonstrated  
227 that both moving nematodes and imaginal discs could be cultured in the device. We showed that  
228 we could harmlessly load the nematode *C. elegans* and culture it for at least 10h (Fig. 5a and  
229 supplementary video S4). The worm remained trapped in the culture chamber, permitting its  
230 imaging under fixed chemical conditions. Additionally, we validated the loading and culture of

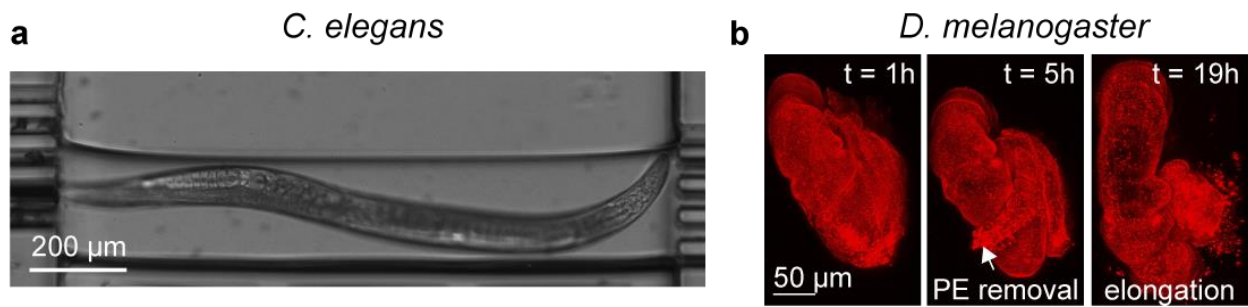


**Figure 5: Culture of moving organism or imaginal discs.** **a.** Moving samples such as the nematode *C. elegans* can be cultured in the device.  $N = 5$  independent experiments. Worms have been culture for 10 hours. **b.** Imaginal discs such as a *drosophila* leg can be loaed, and display normal development in the microfluidic chemostat, as seen by the timing of PE removal and leg elongation.  $N = 3$  independent experiments. The wing has been cultured for 20h.

231 imaginal discs, such as the *Drosophila melanogaster* leg (Fig. 5b, supplementary video S5). The  
 232 smooth manipulation and culture in the chamber allowed us to monitor its development for 20h  
 233 which was similar in the chemostat compared to classical culture conditions<sup>38</sup>. The steady chemical  
 234 environment, produced using syringe pumps, allowed long culture times, typically hard to reach  
 235 with classic culture conditions where culture medium volume is fixed<sup>39</sup>.

236

237 In conclusion, we developed single-cast microfluidic devices for the long-term culture of biological  
 238 samples and their confinement. These devices are ~~easy to use~~, parallelable to increase throughput,  
 239 and can be used to study both the impact of specific chemical conditions and the consequences of  
 240 mechanical compression as well as mechanically characterizing a multicellular spheroid.  
 241 Compressive stress is still poorly understood owing to the lack of tools available to researchers. Our  
 242 device offers an elegant solution to its study.

243

#### 244 **Author contribution**

245 ZBM, TiM, BA and MD designed the culture chambers. ZBM, TiM, BA, LM, RC and MD designed the  
 246 sliding elements. FM, AL, LM and RC helped with microfabrication. TiM, CD, MDL, JGG and MD  
 247 developed cell lines and performed spheroids experiments. ZBM, RDC, CG and MD performed the  
 248 *C. elegans* experiments. ZBM, TaM and MS performed the *D. melanogaster* experiments. SL and MD  
 249 developed the mathematical analysis. ZBM, TiM and MD wrote the manuscript. All authors brought  
 250 corrections to the manuscript.

251

#### 252 **Acknowledgment**

253 The authors would like to thank B. Venzac for critical reading of the manuscript. This work was partly  
 254 supported by the French Renatech network. MD would like to thank Inserm Plan Cancer (Press-Diag-  
 255 Therapy and MechaEvo grants), INCa PLBIO and Cancéropôle Grand Sud-Ouest. This work is partly

256 funded by the European Union (ERC, UnderPressure, grant agreement number 101039998). Views  
257 and opinions expressed are however those of the author(s) only and do not necessarily reflect those  
258 of the European Union or the European Research Council. Neither the European Union nor the  
259 granting authority can be held responsible for them.

260

## 261 **References**

- 262 1. Greco G, Agostini M, Barone S, Cecchini M. Embryo development in dynamic microfluidic  
263 systems. *Sensors Actuators B Chem.* 2017;250:525-532. doi:10.1016/J.SNB.2017.04.186
- 264 2. Letizia MC, Cornaglia M, Trouillon R, et al. Microfluidics-enabled phenotyping of a whole  
265 population of *C. elegans* worms over their embryonic and post-embryonic development at  
266 single-organism resolution. *Microsystems Nanoeng* 2018 41. 2018;4(1):1-11.  
267 doi:10.1038/s41378-018-0003-8
- 268 3. Levario TJ, Zhan M, Lim B, Shvartsman SY, Lu H. Microfluidic trap array for massively parallel  
269 imaging of *Drosophila* embryos. *Nat Protoc* 2013 84. 2013;8(4):721-736.  
270 doi:10.1038/nprot.2013.034
- 271 4. Li X, Valadez A V., Zuo P, Nie Z. Microfluidic 3D cell culture: potential application for tissue-  
272 based bioassays. <https://doi.org/104155/bio12133>. 2012;4(12):1509-1525.  
273 doi:10.4155/BIO.12.133
- 274 5. Mulholland T, McAllister M, Patek S, et al. Drug screening of biopsy-derived spheroids using  
275 a self-generated microfluidic concentration gradient. *Sci Reports* 2018 81. 2018;8(1):1-12.  
276 doi:10.1038/s41598-018-33055-0
- 277 6. Lim W, Park S. A Microfluidic Spheroid Culture Device with a Concentration Gradient  
278 Generator for High-Throughput Screening of Drug Efficacy. *Mol* 2018, Vol 23, Page 3355.  
279 2018;23(12):3355. doi:10.3390/MOLECULES23123355
- 280 7. Huh D, Matthews BD, Mammoto A, Montoya-Zavala M, Hsin HY, Ingber DE. Reconstituting  
281 Organ-Level Lung Functions on a Chip. *Science (80- )*. 2010;328(5986):1662-1668.  
282 doi:10.1126/science.1188302
- 283 8. Bourn MD, Batchelor DVB, Ingram N, et al. High-throughput microfluidics for evaluating  
284 microbubble enhanced delivery of cancer therapeutics in spheroid cultures. *J Control*  
285 *Release*. 2020;326:13-24. doi:10.1016/J.JCONREL.2020.06.011
- 286 9. Paggi CA, Venzac B, Karperien M, Leijten JCH, Le Gac S. Monolithic microfluidic platform for  
287 exerting gradients of compression on cell-laden hydrogels, and application to a model of the  
288 articular cartilage. *Sensors Actuators, B Chem.* 2020;315:127917.



- 289 doi:10.1016/j.snb.2020.127917
- 290 10. Holt LJ, Hallatschek O, Delarue M. Mechano-chemostats to study the effects of compressive  
291 stress on yeast. *Methods Cell Biol.* 2018;147:215-231. doi:10.1016/bs.mcb.2018.06.010
- 292 11. Nia HT, Liu H, Seano G, et al. Solid stress and elastic energy as measures of tumour  
293 mechanopathology. *Nat Biomed Eng.* 2016;1(1):0004. doi:10.1038/s41551-016-0004
- 294 12. Provenzano PP, Cuevas C, Chang AE, Goel VK, Von Hoff DD, Hingorani SR. Enzymatic  
295 Targeting of the Stroma Ablates Physical Barriers to Treatment of Pancreatic Ductal  
296 Adenocarcinoma. *Cancer Cell.* 2012;21(3):418-429. doi:10.1016/j.ccr.2012.01.007
- 297 13. Alessandri K, Sarangi BR, Gurchenkov VV, et al. Cellular capsules as a tool for multicellular  
298 spheroid production and for investigating the mechanics of tumor progression in vitro. *Proc*  
299 *Natl Acad Sci U S A.* 2013;110(37):14843-14848. doi:10.1073/pnas.1309482110
- 300 14. Nam S, Gupta VK, Lee H, et al. Cell cycle progression in confining microenvironments is  
301 regulated by a growth-responsive TRPV4-PI3K/Akt-p27<sup>Kip1</sup> signaling axis. *Sci Adv.*  
302 2019;5(8):eaaw6171. doi:10.1126/sciadv.aaw6171
- 303 15. Rizzuti I, Mascheroni P, Arcucci S, et al. Mechanical Control of Cell Proliferation Increases  
304 Resistance to Chemotherapeutic Agents. *Phys Rev Lett.* 2020;125(12):128103.  
305 <https://journals.aps.org/prl/abstract/10.1103/PhysRevLett.125.128103>
- 306 16. Charras G, Yap AS. Tensile Forces and Mechanotransduction at Cell–Cell Junctions. *Curr Biol.*  
307 2018;28(8):445-457. doi:10.1016/j.cub.2018.02.003
- 308 17. Faurobert E, Bouin A-P, Albiges-Rizo C. Microenvironment, tumor cell plasticity, and cancer.  
309 *Curr Opin Oncol.* 2015;27(1):64-70. doi:10.1097/CCO.000000000000154
- 310 18. Athirasala A, Hirsch N, Buxboim A. Nuclear mechanotransduction: sensing the force from  
311 within. *Curr Opin Cell Biol.* 2017;46:119-127. doi:10.1016/j.ceb.2017.04.004
- 312 19. Santoro M, Lamhamedi-Cherradi S-E, Menegaz BA, Ludwig JA, Mikos AG. Flow perfusion  
313 effects on three-dimensional culture and drug sensitivity of Ewing sarcoma. *Proc Natl Acad*  
314 *Sci.* 2015;112(33):10304-10309. doi:10.1073/pnas.1506684112
- 315 20. Xu J, Mathur J, Vessières E, et al. GPR68 Senses Flow and Is Essential for Vascular  
316 Physiology. *Cell.* 2018;173(3):762-775.e16. doi:10.1016/j.cell.2018.03.076
- 317 21. Heo J, Sachs F, Wang J, Hua SZ. Shear-induced volume decrease in MDCK cells. *Cell Physiol*  
318 *Biochem.* 2012;30(2):395-406. doi:10.1159/000339033
- 319 22. Aoun L, Weiss P, Laborde A, Ducommun B, Lobjois V, Vieu C. Microdevice arrays of high  
320 aspect ratio poly(dimethylsiloxane) pillars for the investigation of multicellular tumour  
321 spheroid mechanical properties. *Lab Chip.* 2014;14(13):2344-2353.

- 322 doi:10.1039/C4LC00197D
- 323 23. Aoun L, Larnier S, Weiss P, et al. Measure and characterization of the forces exerted by  
324 growing multicellular spheroids using microdevice arrays. Oberai AA, ed. *PLoS One*.  
325 2019;14(5):e0217227. doi:10.1371/journal.pone.0217227
- 326 24. Groisman A, Lobo C, Cho H, et al. A microfluidic chemostat for experiments with bacterial  
327 and yeast cells. *Nat Methods*. 2005;2(9):685-689. doi:10.1038/nmeth784
- 328 25. Venzac B, Liu Y, Ferrante I, et al. Sliding walls: a new paradigm for fluidic actuation and  
329 protocol implementation in microfluidics. *Microsystems Nanoeng*. 2020;6(1):1-10.  
330 doi:10.1038/s41378-019-0125-7
- 331 26. Basan M, Risler T, Joanny J-F, Sastre-Garau X, Prost J. Homeostatic competition drives tumor  
332 growth and metastasis nucleation. *HFSP J*. 2009;3(4):265-272. doi:10.2976/1.3086732
- 333 27. Denais CM, Gilbert RM, Isermann P, et al. Nuclear envelope rupture and repair during  
334 cancer cell migration. *Science (80- )*. 2016;352(6283):353-358.  
335 doi:10.1126/SCIENCE.AAD7297/SUPPL\_FILE/PAPV2.PDF
- 336 28. Alric B, Formosa-Dague C, Dague E, Holt L, Delarue Macromolecular M. Macromolecular  
337 crowding limits growth under pressure. *Nat Phys*. Published online November 15, 2022.  
338 doi:10.1101/2021.06.04.446859
- 339 29. Helmlinger G, Netti PA, Lichtenbeld HC, Melder RJ, Jain RK. Solid stress inhibits the growth  
340 of multicellular tumor spheroids. *Nat Biotechnol*. 1997;15(8):778-783.  
341 doi:10.1038/nbt0897-778
- 342 30. Dolega ME, Delarue M, Ingremeau F, Prost J, Delon A, Cappello G. Cell-like pressure sensors  
343 reveal increase of mechanical stress towards the core of multicellular spheroids under  
344 compression. *Nat Commun*. 2017;8:14056. doi:10.1038/ncomms14056
- 345 31. Lee W, Kalashnikov N, Mok S, et al. Dispersible hydrogel force sensors reveal patterns of  
346 solid mechanical stress in multicellular spheroid cultures. *Nat Commun*. 2019;10(1):144.  
347 doi:10.1038/s41467-018-07967-4
- 348 32. Gupta M, Kocgozlu L, Sarangi BR, Margadant F, Ashraf M, Ladoux B. Micropillar substrates:  
349 A tool for studying cell mechanobiology. *Methods Cell Biol*. 2015;125:289-308.  
350 doi:10.1016/BS.MCB.2014.10.009
- 351 33. Guevorkian K, Colbert MJ, Durth M, Dufour S, Brochard-Wyart F. Aspiration of biological  
352 viscoelastic drops. *Phys Rev Lett*. 2010;104(21):218101.  
353 doi:10.1103/PHYSREVLETT.104.218101/FIGURES/4/MEDIUM
- 354 34. Nam S, Gupta VK, Lee H-P, et al. Cell cycle progression in confining microenvironments is

355 regulated by a growth-responsive TRPV4-PI3K/Akt-p27Kip1 signaling axis. *Sci Adv.*  
356 2019;5(8):eaaw6171. doi:10.1126/sciadv.aaw6171

357 35. Cheng G, Tse J, Jain RK, Munn LL. Micro-environmental mechanical stress controls tumor  
358 spheroid size and morphology by suppressing proliferation and inducing apoptosis in cancer  
359 cells. *PLoS One.* 2009;4(2). doi:10.1371/journal.pone.0004632

360 36. Ellis RJ. Macromolecular crowding: An important but neglected aspect of the intracellular  
361 environment. *Curr Opin Struct Biol.* 2001;11(1):114-119. doi:10.1016/S0959-  
362 440X(00)00172-X

363 37. Delarue M, Brittingham GP, Pfeffer S, et al. mTORC1 Controls Phase Separation and the  
364 Biophysical Properties of the Cytoplasm by Tuning Crowding. *Cell.* 2018;174:1-12.  
365 doi:10.1016/j.cell.2018.05.042

366 38. Proag A, Monier B, Suzanne M. Physical and functional cell-matrix uncoupling in a  
367 developing tissue under tension. *Dev.* 2019;146(11). doi:10.1242/DEV.172577/VIDEO-6

368 39. Mandaron P, Gllillermet C, Sengel P. In Vitro Development of Drosophila Imaginal Discs:  
369 Hormonal Control and Mechanism of Evagination. *Integr Comp Biol.* 1977;17(3):661-670.  
370 doi:10.1093/ICB/17.3.661

371 40. Stiernagle T. Maintenance of *C. elegans*. *WormBook*. Published online 2006:1-11.  
372 doi:10.1895/WORMBOOK.1.101.1

373

374

375 **Material and Methods**

376 ***Device microfabrication***

377 The chemostat is made from a two-layer silicon mold. The high-throughput tumor-on-chip is made  
378 from a three-layer silicon mold. For the high-throughput device, we have an initial layer allowing to  
379 create the culture channels. This layer is not present in the chemostat where feeding is ensured  
380 through the sliding element. All layers are created using dry film technology.

381 In order to generate channels alimentation which are characterized by a very tiny section of  $2 \times 2 \mu\text{m}$ ,  
382 an initial layer made of a mix of two SU8 photoresist (SU8-6000.5 and SU8 60005, ratio 1:1) is spin-  
383 coated (speed: 2500rpm, acceleration: 3000rpm/s, time: 30s) with the spin coater Suss Microtec,  
384 on a silicon wafer substrate and cured (2min at  $100^\circ\text{C}$ ). The photoresist is exposed with the MA6  
385 Gen4 machine (I-line 37% at  $300\text{mJ}/\text{cm}^2$ ) with the first mask design and cured ( $100^\circ\text{C}$  for 2min) by  
386 following standard photolithography processes. To create the second layer defining the culture  
387 chamber, a  $100\mu\text{m}$  dry film is laminated above the mold (pressure: 2.5bars, speed: 0.5m/min,  
388 temperature:  $100^\circ\text{C}$  for all lamination), and is exposed using a second mask (I-line 37% at  
389  $240\text{mJ}/\text{cm}^2$ ) and cured ( $100^\circ\text{C}$  during 6min). The last layer is created from a stack lamination of four  
390  $100\mu\text{m}$  dry-film sheets in order to create the  $500\mu\text{m}$  channel used to insert the sliding element.  
391 Then, exposure is performed (I-line 37% at  $2000\text{mJ}/\text{cm}^2$ ) and the mold is cured (PEB of  $100^\circ\text{C}$  during  
392 20min). During exposure steps, particular caution is necessary to align each level with the previous  
393 one.

394 A chemical development in SU8-developper bath is done at the end of the process in order to reveal  
395 the channels. Afterward, a hard-bake is performed to reinforce the mold's mechanical resistance  
396 through time. A perfluorodecyltrichlorosilane (FDTS) self-assembled monolayer is grafted onto the  
397 surface to prevent polydimethylsiloxane (PDMS) adhesion.

398 PDMS is cast onto the mold and cured at  $65^\circ\text{C}$  overnight. The chip is initially sealed with a thin  $50$   
399  $\mu\text{m}$  PDMS layer by plasma activating the two surfaces with oxygen plasma (0.2mBar, 0.7sccm, 25s)  
400 with the Diener Electronics machine in order to have the same material onto the culture chamber  
401 walls. Finally, the whole chip is sealed on a glass slide using the same parameters for plasma O<sub>2</sub>  
402 activation.

403 Once made, the mold surface is controlled by Scanning Electron Microscopy (MEB Hitachi S-4800).  
404 Tension and current are respectively set at 0.6kV and  $8\mu\text{A}$ . To correct astigmatism, magnification is  
405 set at x3000. The image definition is about  $1200 \times 900\text{px}$ .

406

407



408 ***Sliding element fabrication***

409 The sliding element is made of two different levels (300µm and 200µm), using dry film technology,  
410 which allows additive fabrication. Each level required stack lamination of 100µm dry film sheet and  
411 is laminated using the same parameters as the mold fabrication. Starting from a silicon wafer  
412 substrate, three dry films of 100µm are successively laminated on it. This one is exposed with a first  
413 mask (i-line HR 66mW at 1400mJ/cm<sup>2</sup>) and cured (6min at 100°C) by following standard  
414 photolithography processes. The second level is made from two successive laminations of 100µm  
415 dry film sheets. Insolation is done using the second mask (I-line HR 66mW, 900mJ/cm<sup>2</sup>) and the  
416 mold is finally cured (100°C for 3min). While performing the development bath overnight in SU8  
417 developer, all the sliding elements progressively detach from the wafer substrate, as no adhesion  
418 promoter was used. Surface control is done using Scanning Electron Microscopy (MEB Hitachi S-  
419 4800). Finally, a perfluorodecyltrichlorosilane (FDTs) self-assembled monolayer is grafted onto the  
420 surface to prevent cell adhesion.

421

422 ***Cell culture and spheroid formation***

423 A338 cell line<sup>15</sup> derived from a murine pancreatic tumor with an activating mutation of KRas  
424 oncogene (KRas<sup>G12D</sup>) are culture in DMEM (Sigma-Aldrich) supplemented with 10% SVF (Sigma-  
425 Aldrich) and 1% Penicillin-Streptomycin (Sigma-Aldrich), at 37°C and 5% CO<sub>2</sub>. Spheroids are formed  
426 using hanging droplet protocol. Typically, 15µL droplets of a cell suspension (at approximately 13  
427 cells/µL) are dropped on a petri dish cover. To limit evaporation, 7mL of PBS is placed on the other  
428 cover part. Spheroids of 100 µm in diameter are formed in two days. In this study, we transfected  
429 PIP-FUCCI into mouse pancreatic cancer cells (A338), and used HeLa transfected with 40nm-GEMs  
430 (Genetically Encoded Multimeric nanoparticles) as in<sup>37</sup>.

431

432 ***Agarose confinement experiments***

433 A 48-well plate is placed on ice. We prepare a low-melting agarose solution of 2% concentration and  
434 leave it at 37°C to thermalize. 200 µL of medium containing the spheroid of 2/3 days old is then  
435 mixed with 200 µL of 2% low-melting agarose within the pipette. The 400 µL solution is placed on  
436 the 48-well plate on ice, to enable rapid polymerization of agarose at a final concentration of 1%.  
437 We find that this step is necessary to obtain a fully-embedded spheroid: if the polymerization occurs  
438 at room temperature, the spheroid sediments most of the time at the bottom of the well, and is not  
439 embedded in 3D.

440

441 ***C. elegans* culture**

442 We use the *C. elegans* strain N2 (wild type), which is kindly provided by Alfonso Pérez-Escudero. *C.*  
443 *elegans* populations are grown, maintained, and manipulated with standard techniques<sup>40</sup>, except  
444 that the NGM medium is replaced by M9 agar minimal medium (M9 minimal salts supplemented  
445 with 0.2% casamino acids, 0.4% glycerol, 2.0 µg/mL thiamine and 2.5 µg/mL cholesterol).  
446 Synchronized worms are grown on agar plates seeded with a lawn of the bacteria *Ochrobactrum*  
447 *vermis* at 22.5 °C. Adult worms are collected in an Eppendorf tube containing 1 mL of M9 liquid  
448 medium (M9 minimal salts) and then loaded inside the microfluidic chip with a syringe. A single  
449 worm is blocked inside the chamber of the chip, grown for 48 h, and fed with a unidirectional flow  
450 of a culture of *Ochrobactrum vermis* in M9 liquid, at a rate of 500 µL/h.

451

452 ***D. melanogaster* culture and leg preparation**

453 Leg discs from SqhKI[RFP]3B background *D. melanogaster* are dissected at a white pupal stage in  
454 Schneider's insect medium (Sigma-Aldrich, S9895) supplemented with 15% fetal calf serum and  
455 0.5% penicillin-streptomycin, as well as 2 µg/ml 20-hydroxyecdysone (Sigma-Aldrich, H5142). Legs  
456 are then transferred into the microfluidic chamber. Leg discs are imaged with a LSM880 confocal  
457 microscope fitted with a Fast Airyscan module (Carl Zeiss) and equipped with a 40x Water NA-1.2  
458 objective. Stacks of 150 images with a z-step of 1µm are taken every 30 minutes, with a pixel size  
459 of 0.0171µm/pixel. The laser power is set at 1%. Airyscan Z-stacks are processed through the ZEN  
460 software. Max projection images are computed and displayed in Fig. 2.

461

462 ***Loading spheroids and other organisms***

463 First, the chip is filled with DMEM medium supplemented with 10% SVF and 1% Penicillin-  
464 Streptomycin. Then, the sliding element is inserted carefully in the device such that the cavities are  
465 aligned in front of the culture chambers. Spheroids and organisms are taken one by one using a  
466 tubing connected to a syringe. Their injection is done at the inlet localized on the side of the sliding  
467 element channel. Once a spheroid is in the channel, it will go through the sliding element and will  
468 enter the desired chamber for the high-throughput device, or the only chamber for the chemostat.  
469 This step is repeated until all the culture chambers are filled with spheroids for the high-throughput  
470 device. Then, the sliding element is moved so that each chamber is closed with a wall, or aligned  
471 with the slits / holes for feeding. The medium channel is connected to a syringe pump and a flow of  
472 400µL/h is applied.

473

474 ***Imaging conditions***

475 A Zeiss observer microscope is used to perform the acquisition for several days. Biological samples  
476 were observed through a 63x objective. In bright-field, the exposure time was about 100ms with  
477 30% intensity. The environment is fixed at 37°C with 5% CO<sub>2</sub> during the experiment, thanks to a  
478 small incubator (Tokai-hit).

479

480 ***Experiment with the Fucci cell cycle reporter***

481 The PIP-Fucci cell cycle reporter allows us to monitor cell cycle progression through the oscillatory  
482 expression of green and red fluorophores marking different phases of the cell cycle (Fig. 4a). We  
483 recorded 3 z-positions (every 5 μm) of both the GFP and RFP signals (150 ms at 15% intensity), on  
484 top of bright field, during the confined growth of spheroids, with one image every hour. We  
485 performed z-projections of the images and manually counted the green, red, and both green and  
486 red nuclei. We analyzed for each spheroid the total number of tagged cells as well as green alone  
487 cells (G1 cells), to extract the percentage of G1 cells and the percentage of cells in the S, G2, or M  
488 phases of the cell cycle (denoted S/G2/M). Statistics are presented in the caption of Fig. 4b.

489

490 ***Finite element simulations***

491 The geometry of the microfluidic cages including the pressure sensor is simulated using Comsol  
492 multiphysics software with the solid mechanics module in stationary conditions. Once the geometry  
493 of the chamber is created, PDMS (polydimethylsiloxane) is set as a linear elastic material  
494 characterized by Young's modulus of 2 MPa, a Poisson coefficient of 0.49, and a density of 970kg/m<sup>3</sup>.  
495 Concerning boundary conditions, the pressure is applied on the chamber walls which are all free to  
496 deform. Finally, a mesh controlled by physics is applied to the structure and built with tetrahedron  
497 elements. For each applied pressure, the total displacement of the membrane is calculated. A  
498 calibration curve describing the deformation as a function of pressure is used to calibrate all the  
499 experiments.

500

501 ***Surface tension measurement***

502 During the buildup of growth-induced pressure, the aggregate morphs from a spheroid shape to a  
503 cuboid, where the curvature decreases from the radius of the spheroid to the radius of a cell, at a  
504 given mechanical pressure. Denoting  $P_{\text{ext}}^0$  the external pressure,  $P_{\text{int}}$  the internal pressure,  $R$  the  
505 radius of curvature, and  $\gamma$  the surface tension, the Laplace pressure equation can be written

506 
$$P_{\text{int}}^0 = P_{\text{ext}}^0 + \frac{2\gamma}{R_0}$$

507 when the aggregate is a sphere, with  $R_0$  its radius, and

508 
$$P_{\text{int}} = P_{\text{ext}}^0 + P_{\text{mecha}}(R = R_c) = P_{\text{ext}}^0 + \frac{2\gamma}{R_c}$$

509 when the spheroid has morphed into a cuboid shape with curvature radius  $R_c$  which corresponds  
510 to the radius of a cell, and  $P_{\text{mecha}}(R = R_c)$  the mechanical pressure at this time point.

511  $P_{\text{mecha}}(R = R_c)$  is the pressure measured by the pressure sensor. At this surface, the curvature of  
512 the spheroid is  $\sim 0 \mu\text{m}^{-1}$ , the spheroid flattening on the sensor. Given that  $P_{\text{mecha}}(R =$   
513  $R_c) \sim 300\text{Pa}$ , and  $R_c \sim 10\mu\text{m}$ , one gets  $\gamma \sim 1.5 \text{ mN/m}$  as a surface tension value.

514

### 515 ***Genetically-encoded multimeric nanoparticles imaging and diffusion analysis***

516 Experiments are performed on a Leica DM IRB microscope with spinning-disk confocal (Yokogawa  
517 CSU-X1) with a nominal power of 100mW and a Hamamatsu sCMOS camera (Orca flash 4.0 C13440)  
518 with a 63x objective. GEM nanoparticle movies are acquired by illumination with a 488 nm laser at  
519 full power. 30 images are acquired with no delay during 300 ms continual exposure at 100 Hz frame-  
520 rate. Particle tracking is achieved with the FIJI MOSAIC Suite **to extract the trajectories of each**  
521 **particles. For each trajectory, we then compute the single particle time-averaged mean-square**  
522 **displacement, and fit the first 10 points (100ms) with a linear model, to extract a single-particle**  
523 **diffusion coefficient at 100 ms, as in<sup>28</sup>. We then compute the mean and standard error of the mean**  
524 **for the thousands of trajectories collected.**

525

### 526 **Supplementary information**

527

#### 528 ***Title of supplementary videos***

529 **Video S1** – Growth of a multicellular spheroid in the microfluidic chemostat

530 [link to video](#)

531

532 **Video S2** – Loading of a spheroid in the confining chambers through the sliding element

533 [link to video](#)

534

535 **Video S3** – Confined growth of a spheroid and deformation of the suspended membrane with  
536 mechanical growth-induced pressure

537 [link to video](#)



538 **Video S4** – Motion of the nematode *C. elegans* in the microfluidic chemostat

539 [link to video](#)

540

541 **Video S5** – Development of a drosophila leg in the microfluidic chemostat

542 [link to video](#)

543

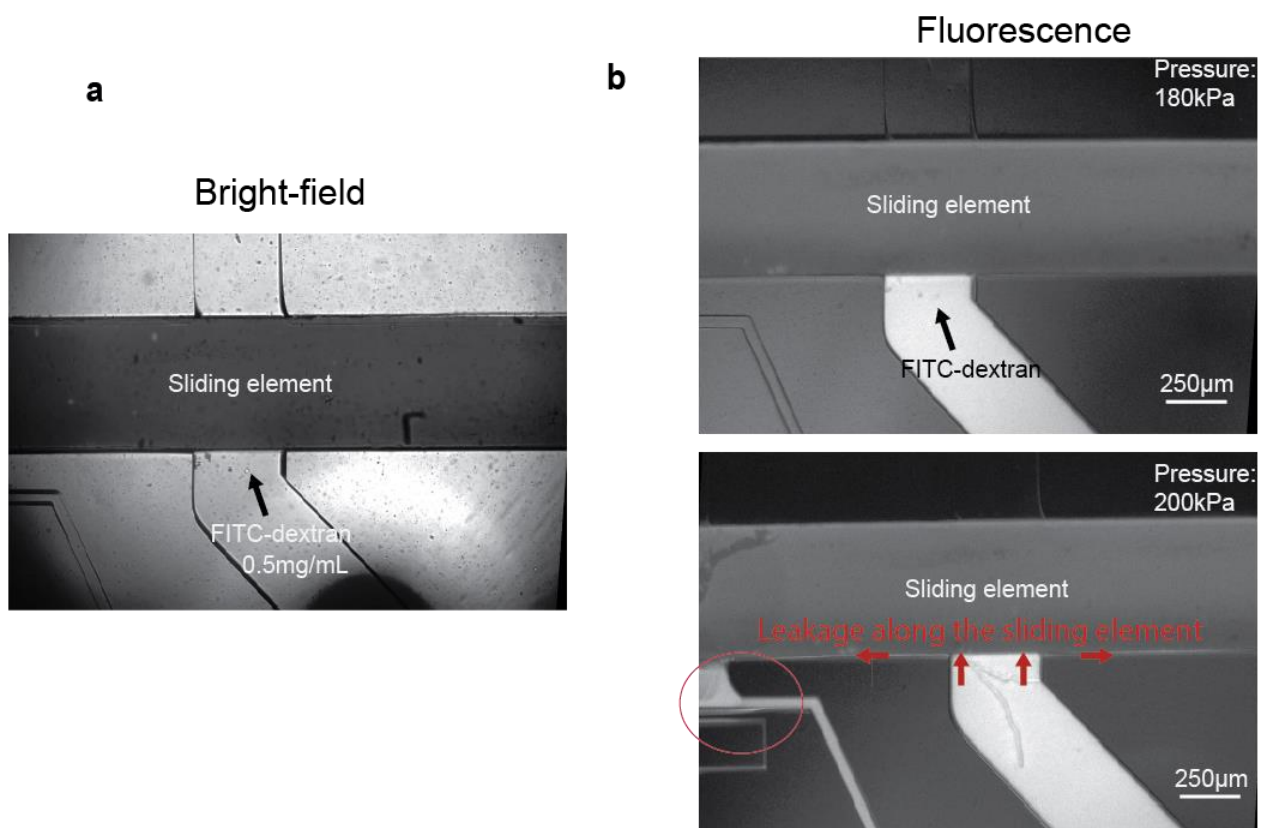


*Figure S1: Increased inlet pressure can lead to leakage in the device, through the sliding element.*

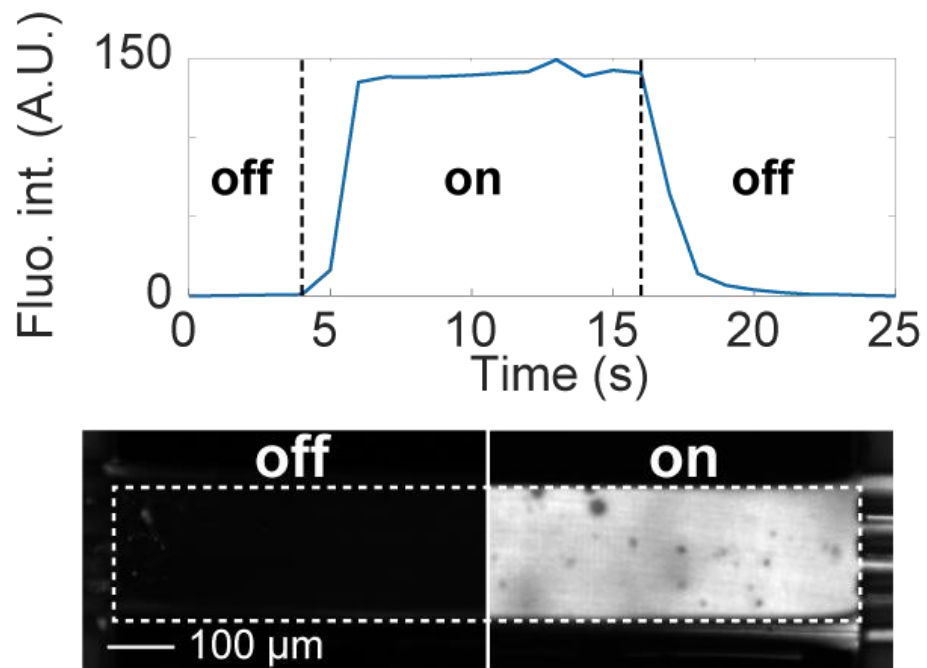
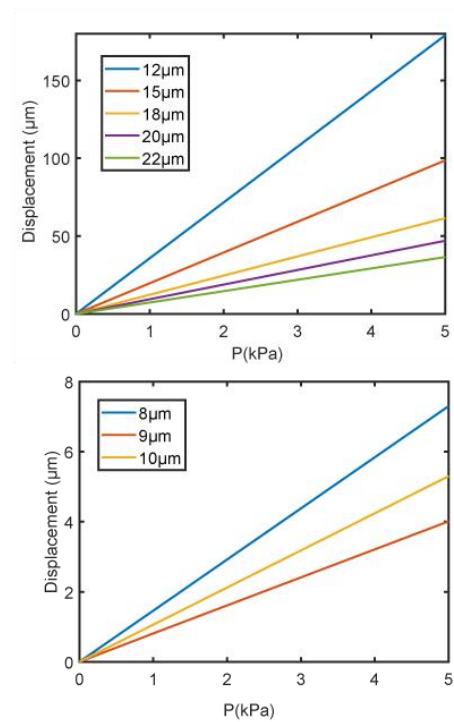
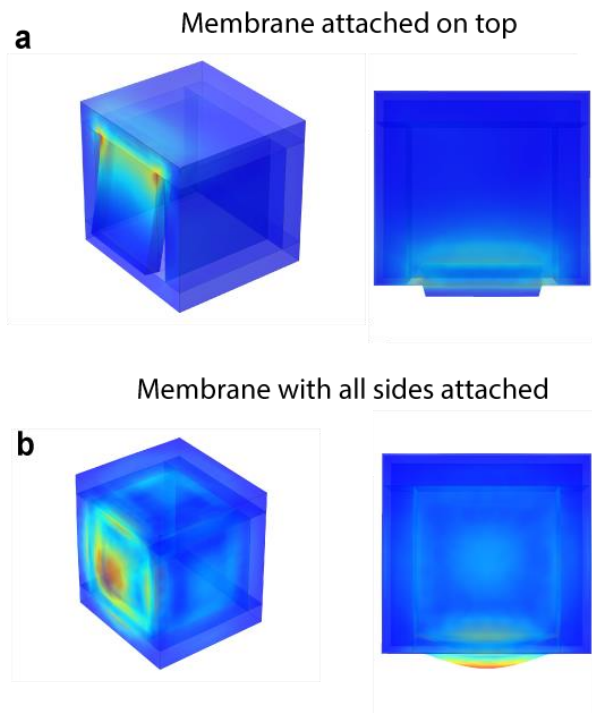
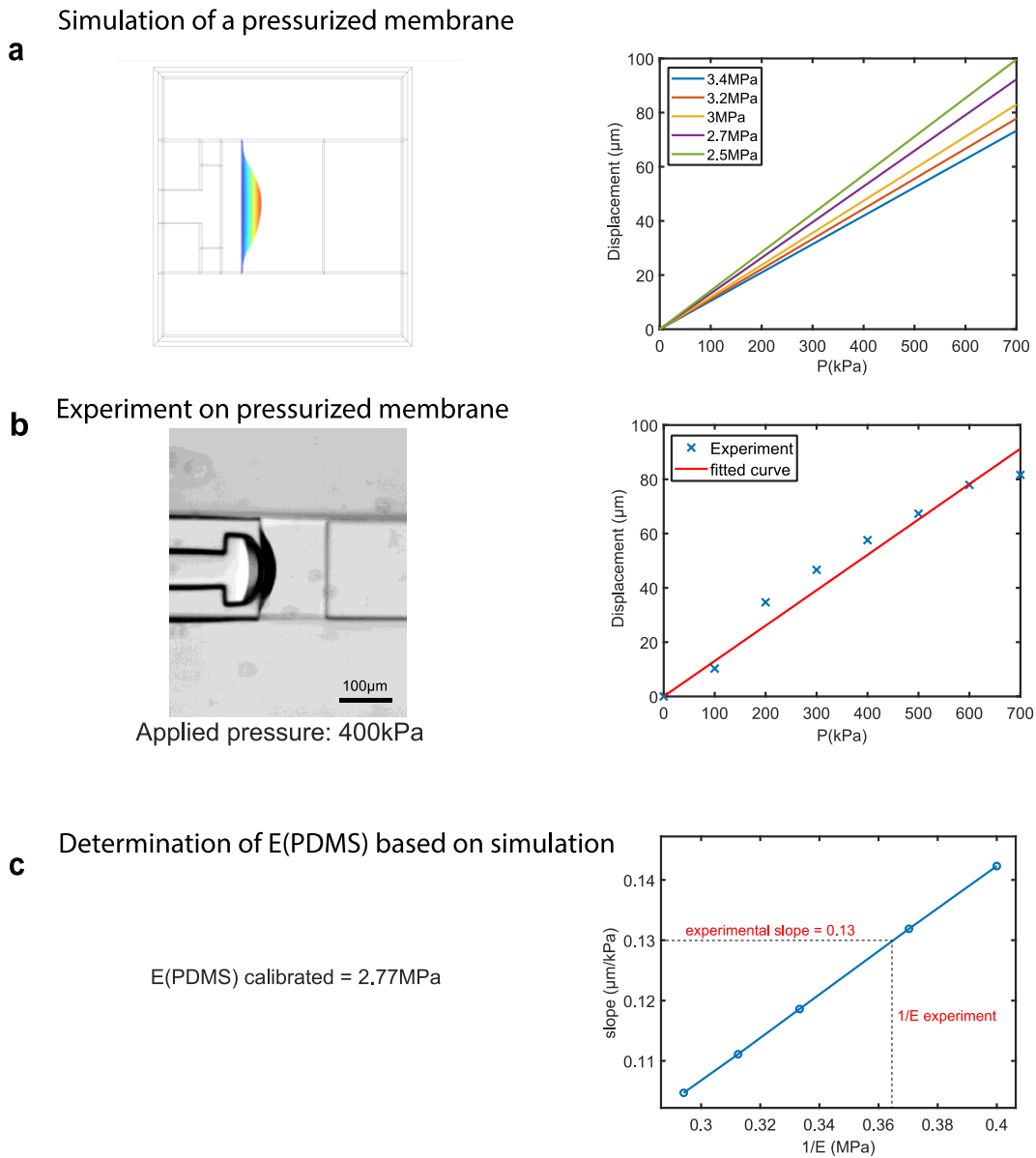


Figure S2: Changing of culture medium inside the device can be achieved within seconds.



**Figure S3.** Finite element simulation of different membrane configurations to measure growth-induced pressure. **a.** Membrane only attached at the top, and **b.** membrane attached to the four sides. We notice the much higher deformability of the membrane only attached at the top.

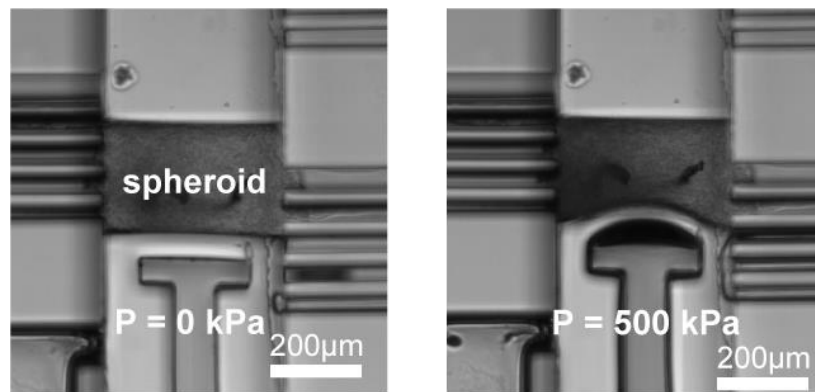




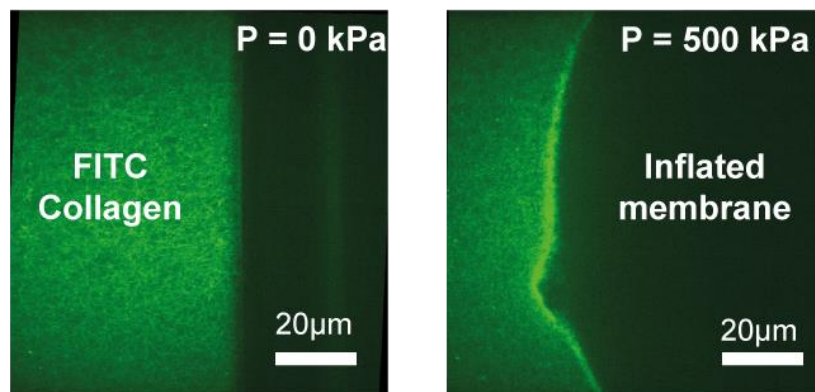
**Figure S4: Calibration of the mechanical properties of the PDMS to use the pressure sensor.** **a.** Simulation and displacement of membrane attached to its four sides as a function of the pressure for different Young's moduli of the material. **b.** Experiment using a membrane attached to its four sides, and its deformation as a function of imposed pressure. **c.** The slope of the deformation of the simulated membrane is inversely proportional to the Young's modulus. We use the simulation to infer the experimental Young's modulus, and use this information together with Fig. S1 to measure growth-induced pressure.

**a**

## Spheroid compression



## Collagen compression

**b**

**Figure S5: Spheroid and hydrogel compression.** Using the membrane attached to every sides, we can impose a give compression onto a loaded sample, either a spheroid (a.) or a collagen hydrogel (b.).

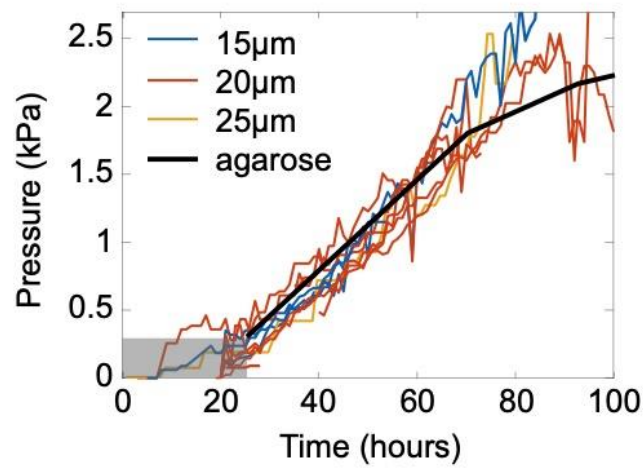


**Figure S6: Agarose confined growth vs. microfluidic confinement.** After the deformation of the spheroid to contact the whole surface of the microfluidic chamber, the spheroid is fully confined. This situation is then comparable to the case where the spheroid is fully embedded as a sphere in agarose. We thus shifted in time (24h) and in pressure (250 Pa) the agarose curve to compare the dynamics of growth-induced pressure buildup with the microfluidic confinement, and observe a similar dynamic. A potential decrease for later points inside agarose is observed, and could potentially be attributed to lesser feeding, the spheroid in agarose also being larger than in the chamber.

### Simulation results for 1kPa pressure

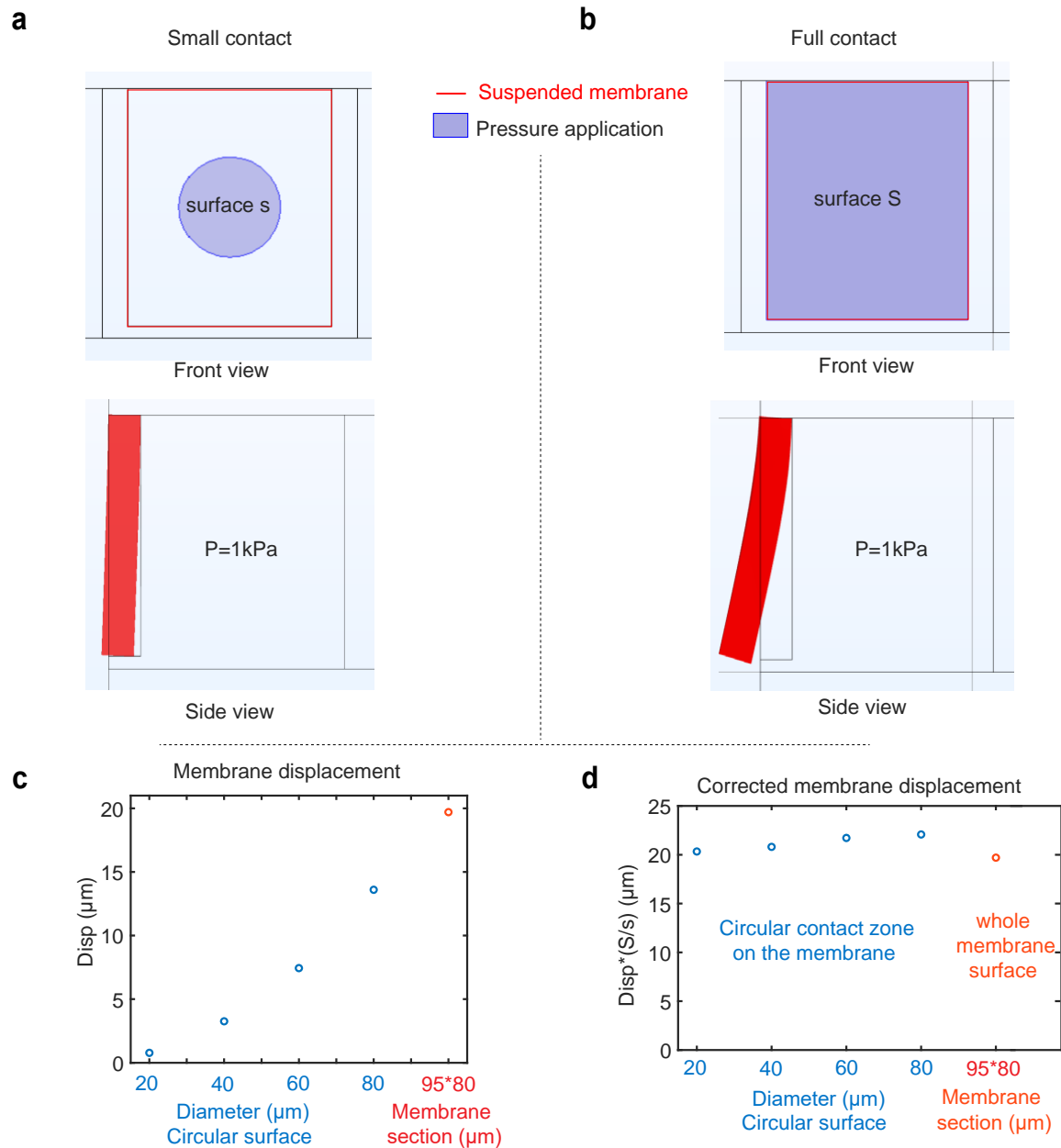
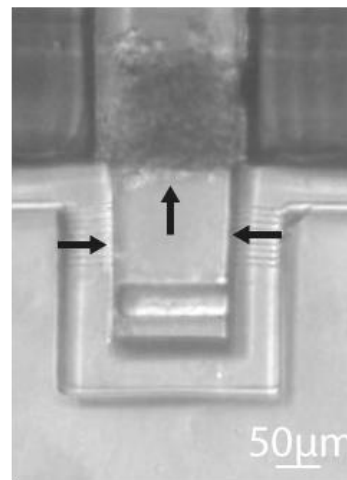
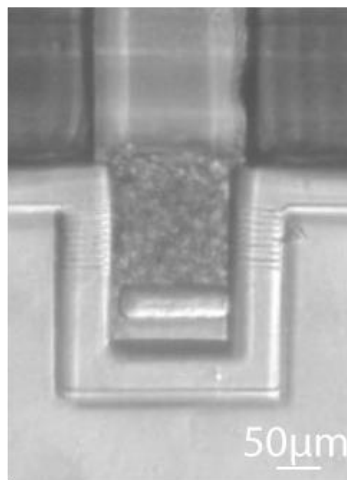
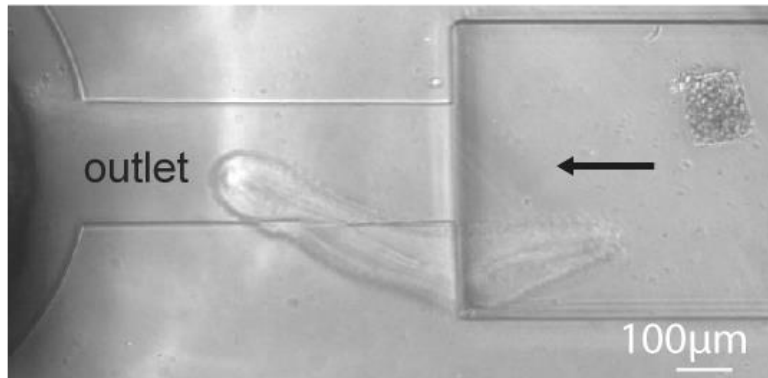


**Figure S7: Correction factor when the spheroid does not fully contact the membrane.** When the aggregate does not fully contact the surface, the pressure is applied on a smaller surface. We performed Finite Element simulations where the contact surface is either a small circle (at early time points, **a**) or fully contact the surface (at confluency, **b**). We observed that displacement increased with surface contact diameter (**c**). We showed that a correction factor of the ratio of the membrane surface to the contact surface needs to be applied (**d**). However, because the membrane does not deform uniformly, this correction factor is not exactly the ratio of the surfaces, and tends to decrease with increased contact surface.

### Spheroid retrieval illustrated in 3 steps



1- Open the chamber 2- Flush spheroid out



3- Flow spheroid towards outlet

*Figure S8 - Procedure to retrieve the spheroid*

### Density measurements

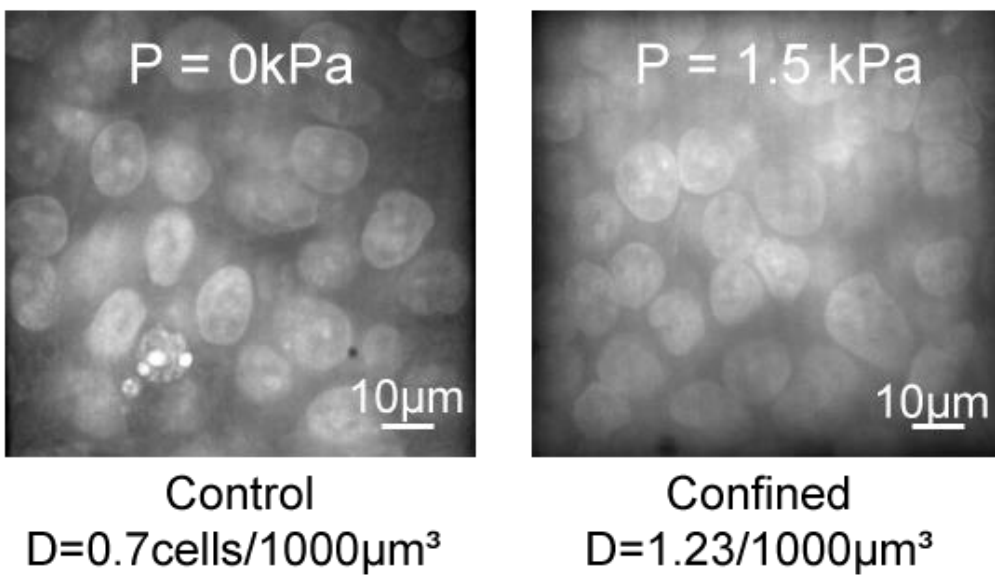


*Figure S9: Cell density increases under confined growth. At the end of an experiment, cells were fixed and nuclei stained with DAPI. 3D stacks were taken and cell density was measured. We observe an almost doubling of cell density under an increase in growth-induced pressure.*